

Nanoparticulate $\text{FeF}_2@\text{C}$ as a Li Battery Conversion Cathode

Bryan R. Wygant, Noah B. Schorr, Igor V. Kolesnichenko, and Timothy N. Lambert*



Cite This: *ACS Appl. Energy Mater.* 2022, 5, 13346–13355



Read Online

ACCESS |

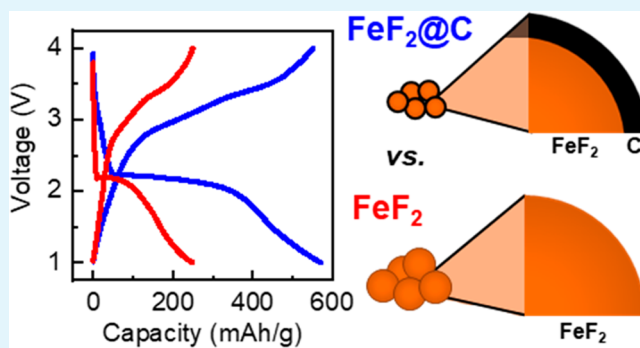
Metrics & More

Article Recommendations

Supporting Information

ABSTRACT: The high theoretical capacity (571 mAh/g) and energy density (1519 Wh/kg) of iron difluoride (FeF_2) make it a promising conversion cathode material for use in Li-based batteries, provided inherent limitations related to material conductivity and reactivity are surmountable. In this work, we report a simple synthesis to produce crystalline FeF_2 particles approximately 35 nm in diameter surrounded by a thin carbon shell ($\text{FeF}_2@\text{C}$) and demonstrate its excellent performance as a cathode in Li metal batteries. Characterization of the $\text{FeF}_2@\text{C}$ shows that the C-shell is 2–3 nm thick and composed of amorphous conjugated carbon with a nitrogen content of 3.8%, largely in the form of pyridinic moieties. When paired with a Li metal anode, the $\text{FeF}_2@\text{C}$ composite cathodes exhibit excellent specific capacity and retention, 634 mAh/g _{$\text{FeF}_2@\text{C}$} after 50 cycles at C/20, compared to 234 mAh/g _{FeF_2} when a cathode containing commercial FeF_2 was used. The material also shows excellent rate performance and, at a 1C charge/discharge rate, demonstrates a capacity greater than that of common intercalation cathodes like LiFePO_4 . We attribute the performance of the $\text{FeF}_2@\text{C}$ to improved lithiation/delithiation behavior due to the nanoscale FeF_2 particles, increased protection from chemical and electrochemical damage, improved conductivity and capacity granted by the C-shell, and additional capacity from the *in situ* formation of FeF_3 during cycling. After electrochemical cycling, *ex situ* analysis of the $\text{FeF}_2@\text{C}$ material shows that while a roughly 2–8 nm cathode electrolyte interphase (CEI) forms on the surface of the particles, the underlying material retains its initial nanostructure and FeF_2 -characteristics.

KEYWORDS: conversion cathode, FeF_2 , core@shell, lithium-metal battery, iron fluoride, energy storage, carbon shell



INTRODUCTION

Due to the ever-increasing energy demands of technologies like portable electronics and electric vehicles, as well as increased development and deployment of renewable energy sources, secondary batteries have become a major focus of battery research.^{1,2} While mature secondary battery chemistries like Pb acid and Li-ion both enjoy widespread use, there has been an increasing demand for batteries which can provide significant energy density with fewer sacrifices due to the weight or volume of the battery components. In response, a range of new battery chemistries are being explored to find a chemistry that avoids such limitations. Among the most promising are high theoretical capacity conversion cathodes composed of earth abundant elements which, when paired with Li metal anodes, would produce high-energy-density batteries competitive with existing chemistries.^{3–5}

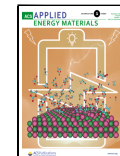
Some of the most promising conversion cathode materials are the iron fluorides, FeF_2 and FeF_3 (collectively referred to as FeF_x), with theoretical capacities of 571 and 712 mAh/g, respectively. FeF_3 has a higher theoretical capacity than FeF_2 but also undergoes a more complex and partially irreversible lithiation/delithiation mechanism.^{6,7} As a result, although it has a lower capacity, the more robust FeF_2 remains an exciting

choice for further study.^{8,9} Ultimately, challenges such as slow lithiation/delithiation kinetics and material stability plague both FeF_x materials and have been the focus of many studies.^{4,10–13} Kinetic limitations have previously been addressed by specialized processing and synthesis, e.g., ball milling,¹⁴ and nanoparticle fabrication,^{9,15} as well as specialized current collectors.¹⁶ In each case, the goal is to use smaller particles to circumvent the kinetic and conductivity limitations inherent to larger particles. Attempts at improving material stability typically rely on protective surface coatings, applied both prior to cell fabrication using *ex situ* techniques,^{17–19} and by careful choice of electrolyte to produce a protective cathode electrolyte interphase (CEI) *in situ*.^{10,11,20} The goal of the coatings is usually 2-fold, both to prevent deleterious reactions at the surface of the material and to inhibit the agglomeration of the FeF_x particles during cycling.^{11,12,17,21}

Received: June 27, 2022

Accepted: October 14, 2022

Published: October 28, 2022



A few techniques, including electrospinning^{21,22} and solvothermal nanoparticle synthesis,^{9,15} have been shown to simultaneously address both nanostructuring and surface coating during synthesis. Unfortunately, nanoparticle syntheses are frequently technically challenging and poorly scalable, while electrospinning produces composite materials with low loadings that limit the energy density of a battery. Microwave synthesis has the potential to circumvent these problems, having been widely used to create nanoscopic materials^{23–26} in a scalable manner.²⁷ It has also been shown to create thin C-shells on the surface of some materials.²⁴ Despite this promise, limited microwave synthesis of metal fluorides has been reported, and only one study has reported even preliminary data regarding the electrochemical performance of such materials.²³

In this work, we address this knowledge gap by using microwave synthesis to create a core@shell FeF₂@C composite composed of nanoscopic FeF₂ particles surrounded by a thin, but encasing, layer of carbon that is only 5.4 wt % of the composite. This is a significantly lower intrinsic C content than that of many similar core@shell FeF₂/C composites and positions the material to have high energy density.^{28,29} We investigate the as-synthesized material using a variety of techniques, including X-ray diffraction spectroscopy (XRD), Raman spectroscopy, X-ray photoelectron spectroscopy (XPS), high-resolution transmission electron microscopy (HRTEM), and others and show that the material is a composite of ~35 nm crystalline FeF₂ particles surrounded by a ~2 nm thick layer of N-containing amorphous aromatic carbon. Tested as a cathode in a Li metal battery, the FeF₂@C shows a capacity of 634 mAh/g_{active} after 50 cycles (at C/20), provides good rate performance (200 mAh/g at 1C-rate), and demonstrates good capacity retention (capacity loss of less than 20 mAh/g over 200 cycles at C/2). Electrochemical impedance spectroscopy (EIS) shows a lower electronic resistance for the FeF₂@C cathode than a commercial FeF₂ material, providing further evidence of the benefits of the C-shell. Physiochemical characterization after cycling shows that a ~2–8 nm layer of inorganic-rich CEI forms on the surface of the composite and that the underlying FeF₂ develops a more FeF₃-like character; electrochemical analysis likewise shows the presence of FeF₃-like species that appear to be largely responsible for increasing the capacity above the theoretical value of 512 mAh/g. Beyond this change, our analysis shows that the composite is otherwise largely stable and promising for use in Li metal batteries.

EXPERIMENTAL SECTION

Materials. All materials were used as received, unless otherwise specified. Iron nitrate nonahydrate (99%, Fisher Scientific) and 1-butyl-3-methylimidazolium tetrafluoroborate [BMIBF₄ (1-butyl-3-methylimidazolium tetrafluoroborate), >98% Sigma-Aldrich] were used for the synthesis of FeF₂@C. Anhydrous FeF₂ powder (97% min, Alfa Aesar) was used for comparison to the synthesized material. Anhydrous 1,2-dimethoxyethane (DME, Sigma-Aldrich) and 1,1,2,2-tetrafluoroethyl-2,2,3,3-tetrafluoropropyl ether (TTE, 99%, Synquest Laboratories) were dried over activated molecular sieves (4 Å, Sigma-Aldrich) for at least 48 h before use. Lithium bis(fluorosulfonyl)imide (LiFSI, 99%, Oakwood Chemical) was dried under vacuum at 100 °C in a heated glovebox antechamber for at least 48 h before use. 1-Methyl-2-pyrrolidone (NMP, anhydrous, Sigma-Aldrich), carbon black (Super P), and polyvinylidene fluoride (PVDF, 5130 Solvay) were used to prepare cathode slurries. 750 μm Li foil (Alfa Aesar) was used as the anode in coin cells.

FeF₂@C Synthesis. Synthesis of the FeF₂@C was performed using a Discover SP Microwave (CEM Corp) using a round-bottom flask attachment and a process adapted from a previous report.²⁴ In a typical synthesis, 400 mg of iron nitrate (0.99 mmol) was dissolved into 4 mL of BMIBF₄ (21.4 mmol) by magnetic stirring in a 10 mL round-bottom flask attached to a Vigreux distillation column sealed with a rubber stopper. The solution was mixed for 1 h, and Ar gas was purged through the headspace of the flask/column during mixing to remove oxygen. After mixing, the Ar was disconnected from the flask/column and the apparatus was placed inside the microwave chamber. A needle attached to a rubber balloon (Ar purged) was inserted into the septum to provide pressure relief during the reaction.

Using the microwave, the solution was heated by increasing the microwave power by 50 W every 30 s until reaching 250 W, and then increasing the power roughly 10 W every 30 s until the solution temperature (measured by an IR thermometer internal to the instrument) reached 290 °C. During the entire process, the solution was magnetically stirred at high speed and the reaction chamber was cooled using compressed air from the microwave, allowing high microwave power to be applied continuously without overheating the reaction solution. This power ramp procedure resulted in a roughly 75 °C/min temperature ramp. After reaching 290 °C, the power was typically lowered to approximately 265 W and the microwave was programmed to maintain the solution at 295 °C for 15 min. During this time, the microwave automatically reduced the applied power if the temperature increased too far, allowing the solution to cool (typically 5–8 °C) before the power was increased again. An example of the solution temperature and microwave power during a typical synthesis is included in Figure S1. After 15 min, the microwave power was turned off and the solution was allowed to cool to approximately 75 °C prior to washing.

After cooling, the resulting black solution was poured into a centrifuge tube and ethanol (anhydrous, Koptec) was added to the solution and mixed. The solution was centrifuged at 3500 rpm on a benchtop centrifuge to collect the black-brown FeF₂@C powder. The powder was redispersed into additional ethanol, and the centrifugation process repeated 5 additional times to remove as much residual BMIBF₄ as possible. The resulting washed FeF₂@C was then dried at 65 °C overnight under vacuum before being cycled into a glovebox for storage and further processing. The reaction typically produced ~90–100 mg of FeF₂@C. Attempts to influence the final carbon content of the composite by varying reaction time, temperature, and reagent concentration were ultimately unsuccessful.

Cathode and Electrolyte Preparation. All cathode preparation was performed in an Ar-filled glovebox (MBraun) with O₂ and H₂O levels <5 ppm. FeF₂@C cathodes were prepared by manually mixing a 5.33:1 weight ratio of FeF₂@C and Super P in an agate mortar and pestle for 5 min. The resulting mixture was then added to a 20 mg/mL solution of PVDF in NMP to create a slurry with a solid composition of 180 mg/mL FeF₂@C+Super P and 20 mg/mL PVDF. This slurry was magnetically mixed for 2 h before being cast onto C-coated Al foil current collectors using a 20 mil doctor blade. After casting, the resulting cathode film was dried on a hot plate at 65 °C overnight. Following drying, 15 mm diameter (1.767 cm²) cathodes were punched out for coin cell fabrication. Commercial FeF₂ cathodes were prepared in a similar manner by replacing the FeF₂@C powder with an equivalent quantity of FeF₂ powder and following the rest of the procedure exactly. FeF₂@C cathodes have a composition of 68.5:17:10 (FeF₂/shell/SuperP/PVDF) by mass and an average areal capacity of 0.71 mAh/cm², while commercial FeF₂ cathodes have a composition of 70:20:10 (FeF₂/SuperP/PVDF) by mass and an average areal capacity of 0.97 mAh/cm².

All electrolyte preparation was performed in an Ar-filled glovebox (MBraun) with O₂ and H₂O levels <0.1 ppm. In a typical preparation, LiFSI (0.468 g, 2.49 mmol) was dissolved into DME (0.271 g, 2.6 mmol) and TTE (1.741 g, 7.47 mmol) to produce a 1:1.2:3 molar ratio of LiFSI/DME/TTE. The solution, henceforth labeled as TTE/DME electrolyte, was stirred overnight and used within 2 months of preparation.

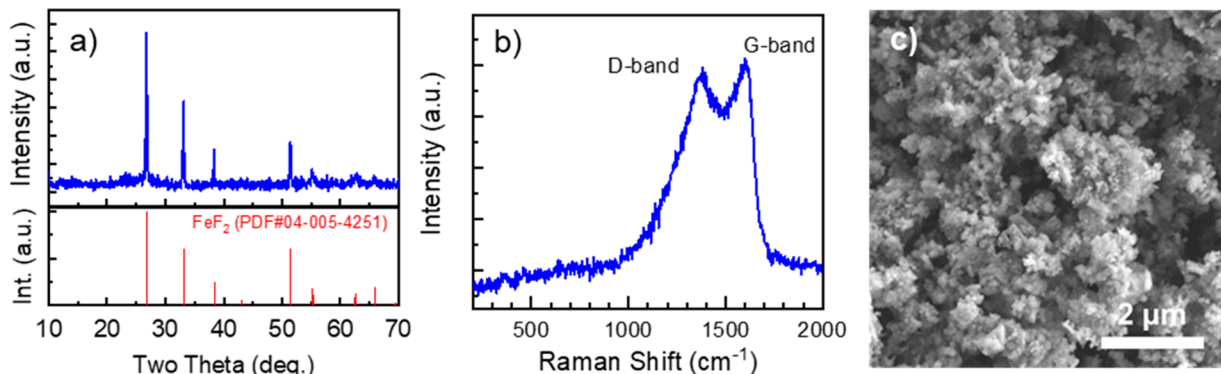


Figure 1. (a) XRD spectrum of FeF₂@C indexed to FeF₂. (b) Raman spectrum of FeF₂@C showing the D- and G-bands of graphitic carbon on the surface. (c) SEM of FeF₂@C showing micron-sized clusters of nanoparticulate material.

Coin Cell Fabrication. All 2032 coin cell fabrication was performed inside an Ar-filled glovebox (MBraun) with O₂ and H₂O levels <0.1 ppm. A single wave spring and 0.7 mm of stainless steel spacers were placed inside the stainless steel anode cap (Hohsen, Japan), and then a 16 mm diameter disk of Li foil was placed on top of the spacers. 70 μL of TTE/DME electrolyte was added to the Li foil, and two 19 mm diameter pieces of polypropylene separator (Celgard 2400) were added on top of the Li foil. A cathode was then placed face down on the separators, and the assembly was capped with a stainless steel cathode cape before being sealed with a coin cell crimper (Hohsen, Japan).

Electrochemical Characterization. Coin cells were cycled galvanostatically between 1 and 4 V at a C-rate of C/20 (relative to the quantity of FeF₂ in the cathode) on a Series 4000 battery tester (Maccor). Average capacities were calculated from triplicate measurements of identically constructed coin cells and reported as the mean ± one standard deviation. Coulombic efficiency was calculated according to eq 1.

$$\text{CE} = \frac{\text{Charge Capacity}_{\text{Cycle } n} \left(\frac{\text{mAh}}{\text{g}} \right)}{\text{Discharge Capacity}_{\text{Cycle } n} \left(\frac{\text{mAh}}{\text{g}} \right)} \times 100\% \quad (1)$$

Rate cycling tests were performed by galvanostatic cycling between 1 and 4 V at C-rates of C/20, C/10, C/5, C/2, and 1C (relative to the quantity of FeF₂ in the cathode) for a limited number of cycles on VMP-300 potentiostat (Biologic). Cyclic voltammetry was also performed on the VMP-300 potentiostat between 1 and 4 V at a sweep rate of 0.1 mV/s.

Physical and Chemical Characterization. Powder XRD spectroscopy was performed on a D2 Phaser (Bruker) spectrometer using a Cu K α radiation source. Raman spectroscopy was performed using a Horiba microscope with a 50× objective and 532 nm laser line excitation source. The instrument was set to a 1200 groove grating, 100 μm slit, and 300 μm hole, with a laser power ~0.25 mW to avoid laser damage (Figure S2). Scanning electron microscopy (SEM) images were collected using a Supra 55VP Field Effect Scanning Electron Microscope (Zeiss) at 3 kV accelerating voltage using a secondary electron detector. Elemental analysis (EA) was performed using a PerkinElmer 2400 CHN-S/O Elemental Analyzer. In a typical run, 2.5–2.75 mg of powder was weighed into a pretreated tin capsule, that was folded into a small, flat square to prevent sample loss and inserted into the instrument for analysis. Annular dark field (ADF) and high-angle annular dark field (HAADF) scanning transmission electron microscopy (STEM) and HRTEM images were captured using a Titan G2 80-200 microscope (FEI Company) operated at 200 kV and equipped with four silicon-drift X-ray detectors (Super XTM). Energy dispersive X-ray spectroscopy (EDX) mapping was performed using a Super-X EDX detector system (4 windowless silicon-drift detectors with a combined solid angle of 0.7 sr), and electron energy loss spectra (EELS) were collected using a Quantum 963

spectrometer (Gatan, Inc.). XPS was performed using a K-alpha X-ray photoelectron spectrometer (Thermo Scientific) equipped with a monochromatic Al source ($K\alpha = 1486.6$ eV). Samples were loaded into the XPS using an inert atmosphere transfer arm to prevent exposure to moisture and oxygen. All spectra were corrected to an adventitious (sp^3) carbon peak at 284.8 eV. For tested STEM and XPS samples, a coin cell was cycled 50 times at C/20 before being opened inside a glovebox. The cathode was harvested from the coin cell and rinsed with roughly 5 mL of dry DME (to remove any residual electrolyte solution) and dried prior to being prepared for further analysis.

RESULTS AND DISCUSSION

XRD, Raman, and SEM Characterization of As-Synthesized FeF₂@C Material. Using microwave synthesis, we were able to produce a nanoscale core–shell FeF₂@C composite in a single step. The iron nitrate acted as the Fe precursor, while the BMIBF₄ ionic liquid acted as both a solvent and the source of C and F. As previously proposed,²⁴ water from the hydrated salt likely reacts with both the Fe(III) in solution to produce Fe₂O₃ and with the BF₄[−] to produce F[−] and hydrated BF₃; this F[−] fluorinates the Fe₂O₃, producing FeF₂. Concurrently, the FeF₂ and Fe₂O₃ act as seeding points for imidazolium decomposition and carbon shell formation. XRD spectroscopy (Figure 1a) confirmed the as-synthesized material is phase-pure FeF₂, without obvious Fe metal, Fe₂O₃, or FeF₃ impurities, or the presence of graphitic carbon peaks near 22° 2θ.³⁰ Based on the sharp peaks, the material is highly crystalline, and the FeF₂ has an average crystallite size of 42 nm by Scherer analysis. Raman spectroscopy showed the D- and G-bands (1380 and 1600 cm⁻¹, respectively) of the carbon shell (Figure 1b), evidence of carbon in the sample.³¹

To gain more structural information about this carbon, we fit the Raman peaks (Figure S3) and calculated the ratio of the peak intensities of the D- and G-bands (I_D/I_G).³⁰ Based on the I_D/I_G ratio for the FeF₂@C material (0.96) and the full width at half-maximum (fwhm) of the G-band (84 cm⁻¹), we can determine that the C-shell is composed of 10 Å or smaller clusters of aromatic carbon.³² We then performed EA of the composite and found the FeF₂@C is roughly 7.2% C, N, and H by mass (5.4 ± 0.5% C, 0.25 ± 0.04% N, and 1.5 ± 0.1% H). As shown in Table S1, N accounts for roughly 3.8% of the atomic composition of the carbonaceous material. While the quantity of N in the C-shell is low, roughly a fifth of that in the BMIBF₄, we believe it likely contributes to the broad D-band observed in the Raman spectra.

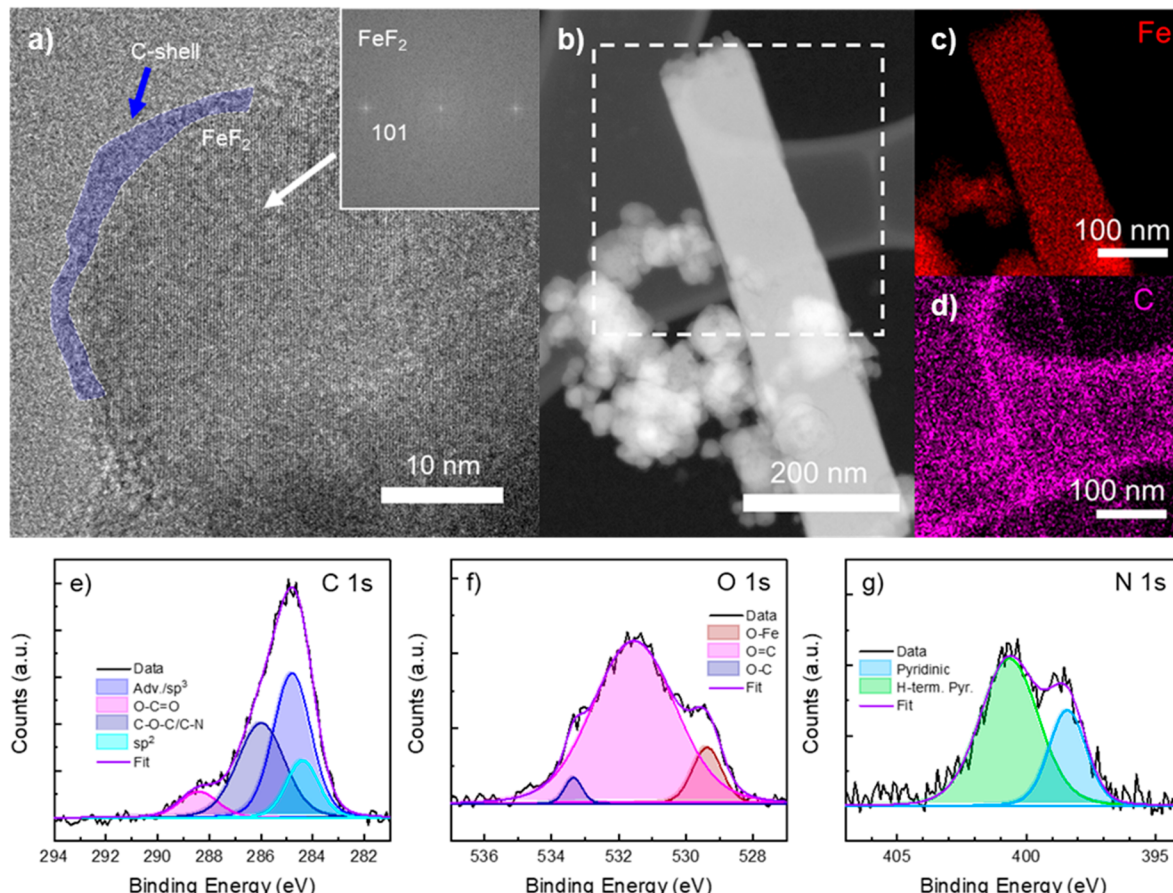


Figure 2. (a) HRTEM image of as-synthesized $\text{FeF}_2@\text{C}$ showing the roughly 2 nm thick amorphous C-shell surrounding the particle. Inset FFT of lattice fringes is indexed to FeF_2 . (b) HAADF STEM image of $\text{FeF}_2@\text{C}$ nanorod and EDX elemental maps for (c) Fe and (d) C from the selected area, confirming the presence of a thin C-shell. (e) C 1s, (f) N 1s, and (g) O 1s XPS spectra showing that the C-shell is composed primarily of oxidized C and pyridinic N species.

Finally, we used SEM to further study the morphology of the $\text{FeF}_2@\text{C}$ (Figure 1c, Figure S4) and found the material is composed of micron-scale agglomerations of primary nanoparticles. While most of the primary particles appear to be roughly spherical, we also observe some nanorod structures ($\sim 1 \mu\text{m}$ long and 150 nm wide) in relatively low abundance (Figure S4b). Together, this initial characterization shows that the microwave-synthesized $\text{FeF}_2@\text{C}$ is composed of a composite of phase-pure nanoparticulate FeF_2 and amorphous N-doped carbon made up of aromatic clusters $< 10 \text{ \AA}$ in size. Unfortunately, this analysis is insufficient to confirm that the composite is truly a nanoscale core@shell material or to provide a more detailed chemical composition of the carbon material itself. As a result, more surface sensitive and higher-resolution analysis using XPS and STEM/HRTEM was performed to gain a more complete picture of this material.

HRTEM, STEM, and XPS Analysis of $\text{FeF}_2@\text{C}$. STEM images of the as-synthesized $\text{FeF}_2@\text{C}$ material (Figure S5) confirm that the material is composed primarily of roughly spherical 35–100 nm particles, as well as a few larger particles (Figure S5b and S6) and nanorods (Figure S5c). While there are also larger particles ($> 200 \text{ nm}$, Figure S6), these constitute a very small number of the particles imaged. Regardless of size, the particles appear to have slight porosity to their structure, possibly due to the formation of NO_x gases from the decomposition of NO_3^- during synthesis, and appear to readily agglomerate into the larger clusters visible in SEM.

STEM imaging of the particles was found to lead to some beam damage and carbon contamination of the samples, prompting us to use less-damaging HRTEM imaging to specifically study the C-shell. In the images, we found a roughly 2–3 nm thick layer of amorphous material (Figure 2a, shaded blue) along the outer edge of the FeF_2 particle, constituting a shell of the amorphous C material observed in the Raman spectroscopy. An uncolorized image of this layer is provided in Figure S7 for improved clarity of this amorphous layer. The composition of the layer is further confirmed by EDX elemental mapping of an FeF_2 nanorod (chosen for its size, to limit beam damage) which shows a thin layer of C surrounding the outer edge of the Fe-rich material (Figure 2b–d). Although larger than the nanoparticles, EDX mapping of the nanorod helps demonstrate the relative uniformity of the C-shell on its surface (shown in Figure S8) more clearly. In both HRTEM and EDX mapping, the C-shell surrounding the FeF_2 core appears to be variable in thickness but conformal across the surface of the particle, and therefore likely to help protect the underlying active material in a manner similar to previous carbon coatings by inhibiting agglomeration and/or uncontrolled surface reactions.^{20,22}

XPS analysis of the as-synthesized $\text{FeF}_2@\text{C}$ material provides further information about both the C-shell and the overall composite (Figure 2e–g and Figures S9 and S10). Beginning with the C-shell, the C 1s region (Figure 2e) contains both sp^2 (284.4 eV) and sp^3 (284.8 eV) hybridized

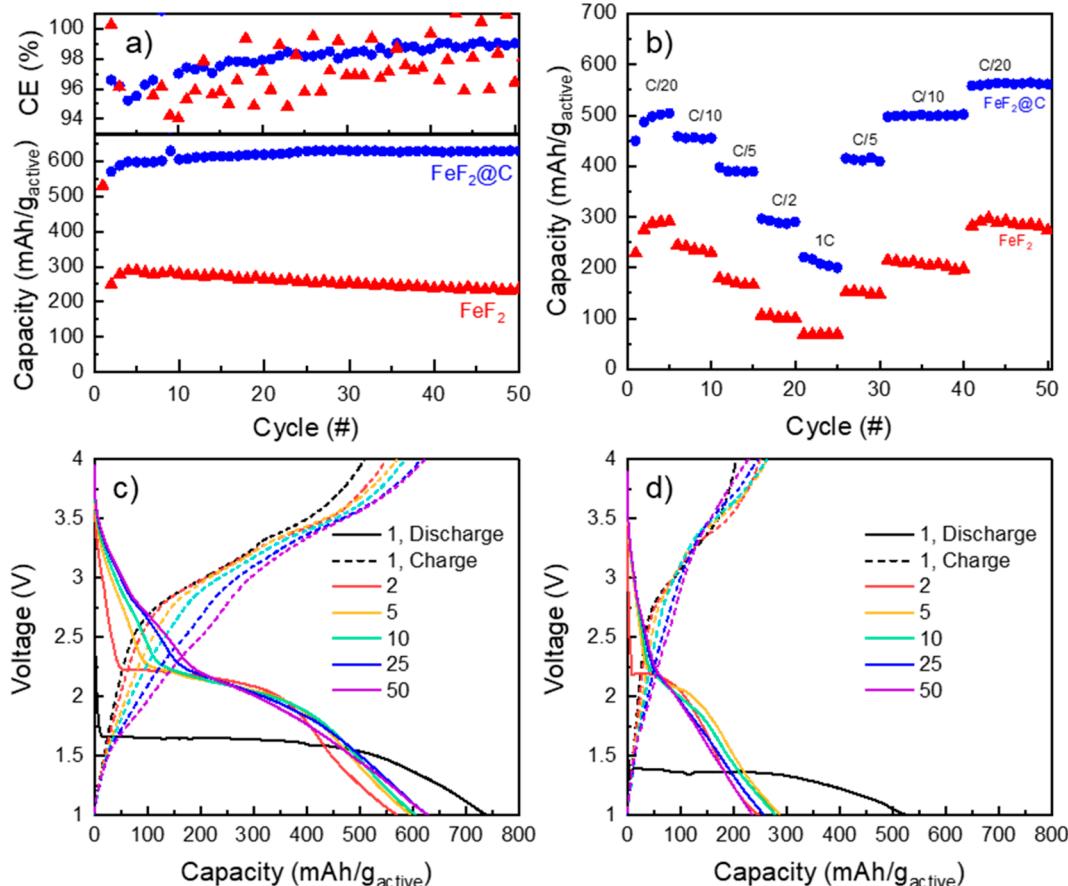


Figure 3. (a) Discharge capacities and Coulombic efficiencies of $\text{FeF}_2@\text{C}$ and FeF_2 (normalized to the quantity of active material), showing improved performance of $\text{FeF}_2@\text{C}$. (b) Rate cycling performance of $\text{FeF}_2@\text{C}$ and FeF_2 at C-rates ranging from C/20 to 1C. Charge/discharge profiles of (c) $\text{FeF}_2@\text{C}$ and (d) FeF_2 at selected cycles showing similar features for both materials.

carbon, in agreement with the Raman spectroscopy (Figure 1b). It also appears to be significantly oxidized, with notable peaks for O—C=O (288.4 eV) and C—O—C/C—N (286 eV) species in the C 1s region, and O=C (531.6 eV) and O—C (533.4 eV) peaks in the O 1s region (Figure 2f).³³ Given the hydrated water present in the iron precursor salt, this oxidation likely occurred during material synthesis. Evidence of surface oxidation of the underlying FeF_2 is also visible in the Fe 2p 3/2 region (Figure S9a), which shows a peak for iron oxide at 710.2 eV³⁴ in addition to peaks for FeF_2 and FeF_3 (711.8 and 713.8 eV, respectively).^{12,35} Importantly though, the surface sensitivity (~ 10 nm) and a lack of Fe_2O_3 in the XRD spectrum indicate that this oxidation is likely confined to the particle surface (~ 7 nm). Finally, XPS analysis also shows that the N in the C-shell consists of pyridinic and H-terminated pyridinic species,³⁶ likely the result of imidazolium decomposition and fragmentation during synthesis.

Elemental quantification based on the survey scan in Figure S10a confirms that the C-shell is composed largely of C (73.3%) with N and O comprising approximately 13% each (Table S1). While both the EA and XPS quantification confirm the C-rich nature of the shell, the extent of N inclusion differs significantly between the two techniques. XPS reports only a 5-fold excess of C relative to N, while EA reports a 25-fold excess. However, given the differences between the techniques and the extreme surface sensitivity of XPS relative to a bulk measurement like EA, we conclude that the EA quantification is more accurate for total elemental quantification. Therefore,

the level of N inclusion in the C-shell is likely lower than XPS suggests. The surface sensitivity of XPS also shows evidence of Na and Si in the material (Figure S10b), and in conjunction with a F 1s peak at 686.6 eV (Figure S9b), this suggests a small Na_2SiF_6 impurity leached from the glass reaction vessel used for synthesis.³⁷ Altogether, XPS characterization shows that the C-shell observed in Figure 2a is composed of partially conjugated, oxidized carbonaceous material containing pyridinic N moieties. With this improved knowledge of the physiochemical properties of the as-synthesized $\text{FeF}_2@\text{C}$ material, we next tested it in Li metal batteries to determine its suitability as a conversion cathode.

Electrochemical Characterization. To study the performance of the $\text{FeF}_2@\text{C}$ as a conversion cathode, we built coin cells using a Li foil anode and a TTE/DME electrolyte previously shown to possess good compatibility with FeF_3 cathodes⁷ and cycled them at C/20 (Figure 3a, Figure S11). As a comparison, we also built coin cells using commercial FeF_2 powder as the active material in the cathodes. These cathodes were prepared following the same procedure as the $\text{FeF}_2@\text{C}$ and act as a control for the effects of cathode preparation and electrolyte choice. The commercial FeF_2 consists of 100 nm FeF_2 crystallites (by Scherer analysis, Figure S12) and contains a small FeF_3 impurity. As shown in Figure 3a, the $\text{FeF}_2@\text{C}$ has a far greater discharge capacity than the commercial FeF_2 after 50 cycles, 634 mAh/g_{active} and 234 mAh/g_{active}, respectively. Furthermore, the $\text{FeF}_2@\text{C}$ material reported here compares very favorably to previously reported FeF_2 cathodes (Table

S2), especially when considering the high loading of FeF_2 relative to other reports. Average capacities from triplicate cells show similar performance (Figure S11). Furthermore, the charge/discharge behavior of the commercial FeF_2 is far more erratic than that of $\text{FeF}_2@C$, leading to more uneven cycling (best demonstrated by the Coulombic efficiencies, Figure 3a).

We also note two important points about the cycling performance and its presentation in this work. First, the C-shell is an intrinsic part of the $\text{FeF}_2@C$ and therefore cannot be physically decoupled from the composite or electrochemically decoupled from the cycling behavior. As a result, we have chosen to report our results per gram of “active” material, here defined as the total mass of the nonbinder and nonconductive additive components of the cathode. As such, the mass of the C-shell is included in our calculations of cathode mass and capacity. Second, and on a related note, on average our $\text{FeF}_2@C$ material shows approximately 108% of the calculated theoretical capacity of FeF_2 . We propose three possible explanations for this extra capacity. First, because the active material (as defined above) contains both FeF_2 and the carbon shell, small variations in quantification by mass could result in notable differences in capacity. Second, both N-free and N-containing amorphous carbons have demonstrated Li storage,^{30,38} and it is possible the C-shell of the material could contribute to the capacity of the composite. However, this explanation is less likely, given the low theoretical capacity of the C-shell (3.5% additional capacity, based on the theoretical capacity of graphite, 372 mAh/g), and the low lithiation potential of most C (below 1 V vs Li). The third, and most likely, explanation for increased capacity is the *in situ* formation of higher-capacity FeF_3 during cycling.

With a theoretical capacity greater than that of FeF_2 (712 mAh/g_{FeF3} vs 571 mAh/g_{FeF2}), the presence of any FeF_3 in the cathode could contribute additional capacity. The dQ/dV plots of the second and 50th discharge cycles of a $\text{FeF}_2@C$ cathode (Figure S13) show that a discharge peak forms near 2.75 V after 50 cycles. This voltage corresponds to the discharge of FeF_3 ,¹¹ and additional spectroscopic evidence for FeF_3 is discussed in a later section. Integration of the area under this peak shows the peak contributes 600× more capacity on the 50th cycle than the second; this additional capacity (~80 mAh/g) largely accounts for the greater-than-theoretical capacity of the cathode. Similar *in situ* formation of FeF_3 from carbon-coated FeF_2 was previously observed in Na-based systems and correlated to superior capacity to FeF_3 -free cathodes,^{39,40} providing additional support for our hypothesis. Regardless of the exact mechanism, even with the additional C mass, $\text{FeF}_2@C$ shows excellent per-g capacity and is a promising material for high-capacity Li metal batteries.

The promise of the composite is also supported by the rate capability of the $\text{FeF}_2@C$ relative to the commercial FeF_2 , as shown in Figure 3b. We found that the $\text{FeF}_2@C$ shows higher capacity and better capacity retention than the commercial FeF_2 at each of the five C-rates tested. Even at 1C, the $\text{FeF}_2@C$ shows more capacity than many commercial intercalation-based cathodes (LCO, NMC, LFP) and cycles at comparable capacity to the C/2 capacity of other nanoscale FeF_2 materials.⁹ Additionally, while both materials show initially little loss of capacity upon returning to slower C-rates (C/10, C/20) after cycling at 1C, only the $\text{FeF}_2@C$ shows stable capacity for the duration of these subsequent cycles. In contrast, the commercial FeF_2 exhibits gradual capacity decay upon returning to slower cycling rates; this likely indicates the

material suffered intrinsic damage at high cycling rates. The smaller size of the primary $\text{FeF}_2@C$ particles relative to the larger commercial FeF_2 particles improves the lithiation/delithiation kinetics of the composite and likely dissuades particle resizing, demonstrating the value of nanoscale FeF_2 material.⁴¹ Furthermore, the $\text{FeF}_2@C$ also performs well relative to a similar FeF_3 material which has been ball milled to produce a nanoscale FeF_3/C composite,⁷ a significantly more involved process than simply mixing the $\text{FeF}_2@C$ with carbon in a mortar and pestle. The material is also stable over longer-term cycling, and the $\text{FeF}_2@C$ lost only 16 mAh/g_{active} after cycling at C/2 for 200 cycles before returning to C/20 (Figure S14). This clearly demonstrates the performance and stability of the $\text{FeF}_2@C$ composite over both tens (Figure 3a) and hundreds of cycles.

Despite the differences in cathode performance, charge-discharge curves (Figure 3c,d) and cyclic voltammograms (CV, Figure S15a,b) show that the nanoscale $\text{FeF}_2@C$ does not initially exhibit significantly different electrochemical profiles than the commercial material. On the first cycle, both materials show a low voltage discharge near 1.5 V that increases to approximately 2.25 V on subsequent cycles (corresponding to the anodic CV and dQ/dV peaks at ~1.75–2 V in Figures S13 and 15). This feature has previously been assigned to the reduction of Fe^{2+} to Fe^0 .^{8,42} On charge, the CVs of both materials show cathodic peaks near 3.0 and 3.5 V, corresponding to the formation of FeF_2 and FeF_3 , respectively.^{8,42} As cycling continues, however, the electrochemical behavior of the two materials diverges. Over 25 cycles, the $\text{FeF}_2@C$ experiences only a gradual broadening and decrease in the current density of the $\text{Fe}^{2+}/\text{Fe}^0$ peak, in addition to the gradual formation of a small reductive peak near 2.7 V (Figure S15a).⁴³ As previously discussed, this feature is attributed to the *in situ* formation and subsequent reduction of FeF_3 during cycling.¹¹ In contrast, the commercial FeF_2 exhibits a much more extensive broadening of the $\text{Fe}^{2+}/\text{Fe}^0$ peak and a significant shift of the peak toward 1.5 V (Figure S15b); despite the presence of FeF_3 in the XRD spectrum (Figure S12), the CV shows it has a minimal electrochemical impact and only a small peak near 2.7 V is observed for the commercial FeF_2 . Previous studies of FeF_2 cathodes have observed similar behavior peak broadening and shifting in the 1.5 V peak and attributed such changes to irreversible changes to the electrodes like the formation and growth of CEI on the surface of the FeF_2 .^{11,44} Given that smaller particles of the $\text{FeF}_2@C$ with higher surface area would ordinarily be expected to exacerbate the effects of CEI growth relative to the larger commercial FeF_2 particles, we propose that the C-shell is protecting the underlying material from significant interfacial reactions with the electrolyte that could disrupt the chemistry or morphology of the inner FeF_2 .

The electrochemical impact of the C-shell can also be clearly seen in EIS Nyquist plots of both materials (Figure 4). The EIS spectrum of the $\text{FeF}_2@C$ cell exhibits two distinct semicircles. We attribute the smaller to charge transfer at the C-shell (R_{shell}) and the larger to the charge transfer resistance (R_{CT}) of the FeF_2 itself. The small diameter of the R_{shell} semicircle indicates that the shell is more electronically conductive than the more resistive FeF_2 interface.⁴⁵ We believe this conductive C-shell is one of the factors that improves the performance of the $\text{FeF}_2@C$ material.⁴⁶ In contrast, the commercial FeF_2 has only a single semicircle for the R_{CT} of the material. It is notably larger than that of the

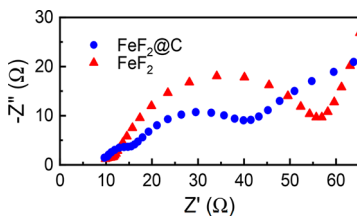


Figure 4. EIS spectra of $\text{FeF}_2@\text{C}$ and FeF_2 displayed as Nyquist plots. The $\text{FeF}_2@\text{C}$ shows both a small semicircle corresponding to the C-shell and a smaller charge transfer, while the FeF_2 shows only a larger charge transfer semicircle.

$\text{FeF}_2@\text{C}$, indicating greater charge transfer resistivity. This agrees with the lower initial discharge potential of the commercial FeF_2 material in Figure 3d and the poor rate performance of the material.

Overall, these results agree with the charge/discharge and CV data for these materials and demonstrate the value of combining a nanoscale material with a protective carbon shell. However, because such electrochemical analysis gives a relatively indirect means of studying physiochemical changes to the $\text{FeF}_2@\text{C}$ material with cycling, we chose to re-examine the material after electrochemical testing using electron microscopy and XPS to determine how the material responds to lithiation/delithiation. More specifically, we examined changes to the particle size/morphology, crystallography, and surface coating using STEM and studied the chemical composition of the newly formed CEI using XPS, of a cathode in the charged state after 50 cycles.

Postcycling Characterization. Particle shape, size, and composition can be significantly altered by electrochemical cycling of conversion cathodes; therefore, we wanted to investigate any changes to the $\text{FeF}_2@\text{C}$ material using STEM and HRTEM. We began by re-examining the material with STEM after 50 cycles at C/20 (Figure S16) and saw few differences when comparing it to uncycled material (Figures S5 and S6). While we do observe a more rounded appearance in some particles after testing that may be related to

reorganization of the material, this appears to be isolated to the larger particles. Furthermore, there is no clear evidence of particle merging, which is likely prevented by the C-shell surrounding the particles.⁹ Therefore, the particles are able to remain nanostructured and retain their improved lithiation/delithiation kinetics.

HRTEM images of the material (Figure 5a) again show that a layer of amorphous material remains at the surface of the crystalline iron fluoride particle (highlighted in blue, uncolored image in Figure S17), but this layer has grown to approximately 4–5 nm in thickness (an additional 2 nm relative to the as-synthesized material). EDX elemental mapping of the material shows that the amorphous layer contains both C and S (Figure 5b–e). While the C could be from both the initial C-shell or the CEI, the S could only have come from decomposition of the FSI^- anion in the electrolyte and, thus, unambiguously demonstrates a CEI layer has formed. From this, we conclude that roughly 2 nm of CEI has formed during testing of the cathode. Additionally, FFT taken from the underlying particle can be indexed to FeF_3 , in agreement with the formation of the previously mentioned Fe^{3+} phase observed in Figures S13 and S15. SAED and EELS analysis (Figures S18 and S19) also show evidence of this Fe^{3+} phase, before and after testing. Importantly, the far greater Fe^{2+} contribution confirms the material remains primarily FeF_2 despite the electrochemical contributions of the FeF_3 phase.⁴⁷ Taken together, we speculate that this FFT indicates the FeF_3 formed *in situ* may consist of single, discrete particles within the larger cathode matrix.

Electrochemical cycling can also have a significant impact on the surface chemistry of conversion cathodes, depositing CEI and potentially impacting the C-shell in our materials. To investigate this, we conducted XPS analysis of both fresh (as-prepared cathodes) and cathodes tested for 50 cycles (Figures S20 and S21). This provided further characterization of the surface C-shell/CEI layer and the changes that cycling induced. The $\text{Fe} 2\text{p } 3/2$ peak is lost after testing (Figure S20a), providing further evidence of CEI growth. Given the roughly 10 nm penetration depth of XPS, this indicates that

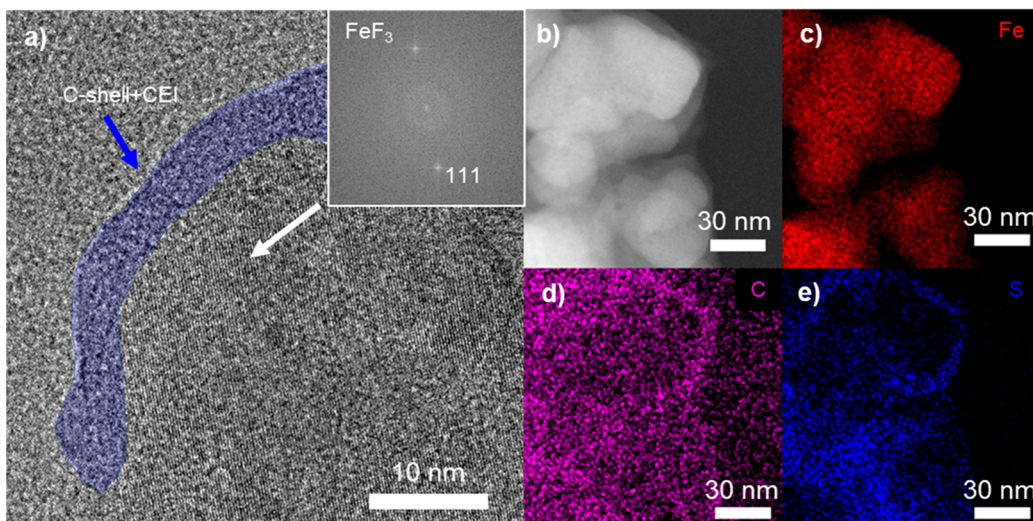


Figure 5. (a) HRTEM image of $\text{FeF}_2@\text{C}$ in a charged state after 50 cycles. The blue shaded area corresponds to the roughly 4 nm thick amorphous C-shell/CEI at the surface of the iron fluoride particles. The inset shows the FFT of the lattice spacings inside the particle corresponding here to FeF_3 . (b) HAADF STEM image of tested $\text{FeF}_2@\text{C}$ and elemental EDX maps of (c) Fe, (d) C, and (e) S. Thin layers of C and S are colocated at the surface of the $\text{FeF}_2@\text{C}$ particles in the C-shell/CEI layer.

the layer may be 6–8 nm thick, with the upper range limited by clear evidence of sp^2 carbon from the C-shell visible in the C 1s region (Figure S20c). We also observe peaks consistent with sulfonyl and sulfonimide species in the S 2p region (166.9/168.1 eV and 168.7/169.8 eV, respectively) confirming the presence of the S-containing CEI layer indicated by EDX mapping.⁹ The N 1s spectra (Figure S20d) also show the presence of sulfonimide species in the CEI,⁹ as well as evidence of pyridinic species in the C-shell that have been oxidized to pyrrolic moieties.³⁶ In addition to these S- and N-species, XPS analysis also shows that the CEI contains LiF (Figure S20b,g) and Li₂O (Figure S20e,g), both of which are common inorganic species in CEI.^{48,49} Overall, XPS analysis of the survey scan in Figure S21 shows that the C-shell/CEI layer is rich in inorganic species (Table S3); Li and O are particularly abundant, which suggests the CEI is rich in Li₂O. This is a feature of CEI formed on cathodes in the TTE/DME electrolyte used in this study, and previous work showed a similar layer was produced on bare FeF₃ electrodes.⁷ Here, the authors concluded that the Li₂O-rich CEI in particular provided an ideal protective barrier which enabled repeated cycling of FeF₃. As Li₂O is known to have reasonable Li⁺ transport properties,⁵⁰ it may act as a protective Li⁺-permeable barrier for the FeF₂@C particles during cycling. In conjunction with the C-shell, such a CEI would be expected to allow Li⁺ transport to the FeF₂ surface while preventing deleterious reactions.

Together, this characterization of the cycled FeF₂@C material shows that a relatively thin (~2–8 nm) CEI rich in inorganic materials forms on the surface of the pre-existing C-shell during electrochemical cycling. The underlying iron fluoride material remains primarily FeF₂ but exhibits some overoxidation to FeF₃. STEM imaging of the cycled composite shows that the particles themselves do not appear to experience significant changes in morphology or size. This suggests the C-shell inhibits the agglomeration and particle growth that can accompany processes such as cycling of nanoscopic battery materials and Oswalt ripening.⁵¹ Overall, we conclude that microwave synthesis of FeF₂@C results in a favorable combination of nanoscale particles and a protective C-shell, and that this combination results in improved cycling behavior when the material is used as a conversion cathode in Li-based batteries.

CONCLUSIONS

In this work, we have demonstrated the microwave synthesis of a composite of nanoscopic FeF₂ particles surrounded by an amorphous carbon shell and its superior use as a FeF_x conversion cathode for use in Li batteries. While XRD and Raman spectroscopy found the material to be a phase-pure FeF₂ surrounded by amorphous carbon, further characterization by HRTEM/STEM and XPS confirmed the presence of ~30–50 nm FeF₂ particles surrounded by a 2–3 nm thick N-doped conjugated C. When tested as a cathode versus a Li metal anode, the nanoscale FeF₂@C provides a capacity of 634 mAh/g_{active} after 50 cycles at C/20, compared to 234 mAh/g_{active} for a similarly prepared commercial FeF₂ material. The additional capacity of the FeF₂@C batteries is attributed to the formation of FeF₃ during electrochemical cycling. The FeF₂@C material also shows superior rate capacity to the commercial FeF₂, and EIS spectra indicate that the C-shell corresponds to reduced R_{CT} , indicative of improved lithiation/delithiation kinetics. Postcycling characterization by HRTEM shows the

growth of an approximately 1–2 nm layer of CEI after 50 cycles, composed largely of inorganic materials like Li₂O based on XPS spectra, but no increase in FeF₂@C particle size from multiparticle agglomeration; it also confirms the presence of FeF₃ in the material. Overall, the combination of a nanoscale FeF₂ material with a thin carbon shell results in a composite with excellent performance as a Li battery cathode, making microwave synthesis of similar materials an exciting path forward to producing promising conversion cathodes.

ASSOCIATED CONTENT

Supporting Information

Representative temperature and microwave power profiles from typical synthesis of FeF₂@C, photographs of FeF₂@C samples after Raman analysis, Raman spectra with individual components fit, table of elemental composition by elemental analysis and XPS, additional SEM images of FeF₂@C, additional STEM images of FeF₂@C prior to testing, uncolorized HRTEM images of FeF₂@C before and after testing, XPS spectra of as-synthesized FeF₂@C, average capacity of triplicate FeF₂@C and commercial FeF₂ batteries, XRD spectrum of commercial FeF₂, dQ/DV of 1st and 50th cycles of FeF₂@C, cyclic voltammograms of FeF₂@C and commercial FeF₂, SAED spectra of FeF₂@C, EELS spectra of FeF₂@C, table of elemental composition of CEI on FeF₂@C. The Supporting Information is available free of charge at <https://pubs.acs.org/doi/10.1021/acsaem.2c01988>.

Additional results such as temperature and power profiles, photographs of samples, Raman spectra, XPS spectra, XRD spectra, SAED spectra, and EELS spectra (PDF)

AUTHOR INFORMATION

Corresponding Author

Timothy N. Lambert – Department of Photovoltaics and Materials Technology, Sandia National Laboratories, Albuquerque, New Mexico 87185, United States;
✉ orcid.org/0000-0002-2359-2876; Email: tnlambe@sandia.gov

Authors

Bryan R. Wygant – Department of Photovoltaics and Materials Technology, Sandia National Laboratories, Albuquerque, New Mexico 87185, United States;
✉ orcid.org/0000-0003-1924-7831

Noah B. Schorr – Department of Photovoltaics and Materials Technology, Sandia National Laboratories, Albuquerque, New Mexico 87185, United States; [✉ orcid.org/0000-0002-1582-8594](https://orcid.org/0000-0002-1582-8594)

Igor V. Kolesnichenko – Department of Photovoltaics and Materials Technology, Sandia National Laboratories, Albuquerque, New Mexico 87185, United States;
✉ orcid.org/0000-0002-9786-4053

Complete contact information is available at:
<https://pubs.acs.org/10.1021/acsaem.2c01988>

Notes

The authors declare no competing financial interest.

ACKNOWLEDGMENTS

This paper describes objective technical results and analysis. Any subjective views or opinions that might be expressed in

the paper do not necessarily represent the views of the U.S. Department of Energy or the United States Government. This work was supported by the Laboratory Directed Research and Development program at Sandia National Laboratories, a multimission laboratory managed and operated by National Technology and Engineering Solutions of Sandia, LLC., a wholly owned subsidiary of Honeywell International, Inc., for the U.S. Department of Energy's National Nuclear Security Administration under contract DE-NA-0003525. This work was performed, in part, at the Center for Integrated Nanotechnologies, an Office of Science User Facility operated for the U.S. Department of Energy (DOE) Office of Science. The authors would like to thank Dr. Samantha Rosenberg for her assistance collecting the XPS data, Dr. Paul Kotula for his assistance collecting the STEM and EELS data, and Sara Dickens for her assistance collecting the SEM data.

■ REFERENCES

- (1) Li, M.; Lu, J.; Chen, Z.; Amine, K. 30 Years of Lithium-Ion Batteries. *Adv. Mater.* **2018**, No. e1800561.
- (2) Dunn, B.; Kamath, H.; Tarascon, J. M. Electrical energy storage for the grid: a battery of choices. *Science* **2011**, 334 (6058), 928–35.
- (3) Wu, F.; Yushin, G. Conversion cathodes for rechargeable lithium and lithium-ion batteries. *Energy Environ. Sci.* **2017**, 10 (2), 435–459.
- (4) Wang, L.; Wu, Z.; Zou, J.; Gao, P.; Niu, X.; Li, H.; Chen, L. Li-free Cathode Materials for High Energy Density Lithium Batteries. *Joule* **2019**, 3 (9), 2086–2102.
- (5) Nitta, N.; Wu, F.; Lee, J. T.; Yushin, G. Li-ion battery materials: present and future. *Mater. Today* **2015**, 18 (5), 252–264.
- (6) Hua, X.; Eggeman, A. S.; Castillo-Martinez, E.; Robert, R.; Geddes, H. S.; Lu, Z.; Pickard, C. J.; Meng, W.; Wiaderek, K. M.; Pereira, N.; Amatucci, G. G.; Midgley, P. A.; Chapman, K. W.; Steiner, U.; Goodwin, A. L.; Grey, C. P. Revisiting metal fluorides as lithium-ion battery cathodes. *Nat. Mater.* **2021**, 20 (6), 841–850.
- (7) Wygant, B. R.; Merrill, L. C.; Harrison, K. L.; Talin, A. A.; Ashby, D. S.; Lambert, T. N. The Role of Electrolyte Composition in Enabling Li Metal-Iron Fluoride Full-Cell Batteries. *Adv. Sci.* **2022**, 9 (12), No. e2105803.
- (8) Huang, Q.; Turcheniuk, K.; Ren, X.; Magasinski, A.; Song, A.-Y.; Xiao, Y.; Kim, D.; Yushin, G. Cycle stability of conversion-type iron fluoride lithium battery cathode at elevated temperatures in polymer electrolyte composites. *Nat. Mater.* **2019**, 18 (12), 1343–1349.
- (9) Xiao, A. W.; Lee, H. J.; Capone, I.; Robertson, A.; Wi, T.-U.; Fawdon, J.; Wheeler, S.; Lee, H.-W.; Grobert, N.; Pasta, M. Understanding the conversion mechanism and performance of monodisperse FeF₂ nanocrystal cathodes. *Nat. Mater.* **2020**, 19 (6), 644–654.
- (10) Senoh, H.; Matsui, K.; Shikano, M.; Okumura, T.; Kiuchi, H.; Shimoda, K.; Yamanaka, K.; Ohta, T.; Fukunaga, T.; Sakaue, H.; Matsubara, E. Degradation Mechanism of Conversion-Type Iron Trifluoride: Toward Improvement of Cycle Performance. *ACS Appl. Mater. Interfaces* **2019**, 11 (34), 30959–30967.
- (11) Huang, Q.; Turcheniuk, K.; Ren, X.; Magasinski, A.; Gordon, D.; Bensalah, N.; Yushin, G. Insights into the Effects of Electrolyte Composition on the Performance and Stability of FeF₂ Conversion-Type Cathodes. *Adv. Energy Mater.* **2019**, 9 (17), 1803323.
- (12) Sina, M.; Thorpe, R.; Rangan, S.; Pereira, N.; Bartynski, R. A.; Amatucci, G. G.; Cosandey, F. Investigation of SEI Layer Formation in Conversion Iron Fluoride Cathodes by Combined STEM/EELS and XPS. *J. Phys. Chem. C* **2015**, 119 (18), 9762–9773.
- (13) Kitajou, A.; Yamagishi, H.; Katayama, M.; Yoshii, K.; Shikano, M.; Sakaue, H.; Okada, S. Elucidation of discharge-charge reaction mechanism of FeF₂ cathode aimed at efficient use of conversion reaction for lithium-ion batteries. *J. Electroanal. Chem.* **2022**, 920, 116577.
- (14) Badway, F.; Pereira, N.; Cosandey, F.; Amatucci, G. G. Carbon-Metal Fluoride Nanocomposites. *J. Electrochem. Soc.* **2003**, 150 (9), A1209.
- (15) Guntlin, C. P.; Zünd, T.; Kravchyk, K. V.; Wörle, M.; Bodnarchuk, M. I.; Kovalenko, M. V. Nanocrystalline FeF₃ and MF₂ (M = Fe, Co, and Mn) from metal trifluoroacetates and their Li(Na)-ion storage properties. *J. Mater. Chem. A* **2017**, 5 (16), 7383–7393.
- (16) Liu, S.; Chen, J.; Su, Y.; Zheng, C.; Zhu, D.; Zhang, X.; Zhou, X.; Ouyang, R.; Huang, Q.; He, Y.; Tang, L.; Li, S.; Qiu, Y.; Wang, G.; Tang, Y.; Zhang, L.; Huang, Q.; Huang, J. Exploiting the Iron Difluoride Electrochemistry by Constructing Hierarchical Electron Pathways and Cathode Electrolyte Interface. *Small* **2022**, 18 (28), No. e2202006.
- (17) Kim, S.; Liu, J.; Sun, K.; Wang, J.; Dillon, S. J.; Braun, P. V. Improved Performance in FeF₂ Conversion Cathodes through Use of a Conductive 3D Scaffold and Al₂O₃ ALD Coating. *Adv. Funct. Mater.* **2017**, 27 (35), 1702783.
- (18) Basa, A.; Wojtulewski, S.; Kalska-Szostko, B.; Perkowski, M.; Gonzalo, E.; Chernyayeva, O.; Kuhn, A.; García-Alvarado, F. Carbon coating of air-sensitive insulating transition metal fluorides: An example study on α -Li₂FeF₆ high-performance cathode for lithium ion batteries. *J. Mater. Sci. Technol.* **2020**, 55, 107–115.
- (19) Li, J.; Meng, Y.; Wang, Y.; Li, X.; Lai, Y.; Guo, Y.; Wen, X.; Xiao, D. The fluorination-assisted dealloying synthesis of porous reduced graphene oxide-FeF₂@ carbon for high-performance lithium-ion battery and the exploration of its electrochemical mechanism. *Inorganic Chemistry Frontiers* **2021**, 8 (13), 3273–3283.
- (20) Zhao, E.; Borodin, O.; Gao, X.; Lei, D.; Xiao, Y.; Ren, X.; Fu, W.; Magasinski, A.; Turcheniuk, K.; Yushin, G. Lithium-Iron (III) Fluoride Battery with Double Surface Protection. *Adv. Energy Mater.* **2018**, 8 (26), 1800721.
- (21) Sun, Z.; Fu, W.; Liu, M. Z.; Lu, P.; Zhao, E.; Magasinski, A.; Liu, M.; Luo, S.; McDaniel, J.; Yushin, G. A nanoconfined iron(iii) fluoride cathode in a NaDFOB electrolyte: towards high-performance sodium-ion batteries. *J. Mater. Chem. A* **2020**, 8 (7), 4091–4098.
- (22) Fu, W.; Zhao, E.; Sun, Z.; Ren, X.; Magasinski, A.; Yushin, G. Iron Fluoride-Carbon Nanocomposite Nanofibers as Free-Standing Cathodes for High-Energy Lithium Batteries. *Adv. Funct. Mater.* **2018**, 28 (32), 1801711.
- (23) Schmitz, A.; Schutte, K.; Ilievski, V.; Barthel, J.; Burk, L.; Mulhaupt, R.; Yue, J.; Smarsly, B.; Janiak, C. Synthesis of metal-fluoride nanoparticles supported on thermally reduced graphite oxide. *Beilstein J. Nanotechnol.* **2017**, 8, 2474–2483.
- (24) Jacob, D. S.; Bitton, L.; Grinblat, J.; Felner, I.; Koltypin, Y.; Gedanken, A. Are Ionic Liquids Really a Boon for the Synthesis of Inorganic Materials? A General Method for the Fabrication of Nanosized Metal Fluorides. *Chem. Mater.* **2006**, 18 (13), 3162–3168.
- (25) Schutte, K.; Barthel, J.; Endres, M.; Siebels, M.; Smarsly, B. M.; Yue, J.; Janiak, C. Synthesis of Metal Nanoparticles and Metal Fluoride Nanoparticles from Metal Amidinate Precursors in 1-Butyl-3-Methylimidazolium Ionic Liquids and Propylene Carbonate. *ChemistryOpen* **2017**, 6 (1), 137–148.
- (26) Sun, Z.; Lin, H.; Zhang, F.; Yang, X.; Jiang, H.; Wang, Q.; Qu, F. Rapid microwave-assisted synthesis of high-rate FeS₂ nanoparticles anchored on graphene for hybrid supercapacitors with ultrahigh energy density. *J. Mater. Chem. A* **2018**, 6 (30), 14956–14966.
- (27) Yin, H.; Yamamoto, T.; Wada, Y.; Yanagida, S. Large-scale and size-controlled synthesis of silver nanoparticles under microwave irradiation. *Mater. Chem. Phys.* **2004**, 83 (1), 66–70.
- (28) Butova, V. V.; Aboraia, A. M.; Shapovalov, V. V.; Dzhangiryan, N. A.; Papkovskaya, E. D.; Ilin, O. I.; Kubrin, S. P.; Guda, A. A.; Soldatov, A. V. Iron (II) fluoride cathode material derived from MIL-88A. *J. Alloys Compd.* **2022**, 916, 165438.
- (29) Gordon, D.; Huang, Q.; Magasinski, A.; Ramanujapuram, A.; Bensalah, N.; Yushin, G. Mixed Metal Difluorides as High Capacity Conversion-Type Cathodes: Impact of Composition on Stability and Performance. *Adv. Energy Mater.* **2018**, 8 (19), 1800213.
- (30) Pender, J. P.; Guerrera, J. V.; Wygant, B. R.; Weeks, J. A.; Ciufo, R. A.; Burrow, J. N.; Walk, M. F.; Rahman, M. Z.; Heller, A.; Mullins,

- C. B. Carbon Nitride Transforms into a High Lithium Storage Capacity Nitrogen-Rich Carbon. *ACS Nano* **2019**, *13* (8), 9279–9291.
- (31) Schorr, N. B.; Jiang, A. G.; Rodriguez-Lopez, J. Probing Graphene Interfacial Reactivity via Simultaneous and Colocalized Raman-Scanning Electrochemical Microscopy Imaging and Interrogation. *Anal. Chem.* **2018**, *90* (13), 7848–7854.
- (32) Schwan, J.; Ulrich, S.; Batori, V.; Ehrhardt, H.; Silva, S. R. P. Raman spectroscopy on amorphous carbon films. *J. Appl. Phys.* **1996**, *80* (1), 440–447.
- (33) Zhou, J.-H.; Sui, Z.-J.; Zhu, J.; Li, P.; Chen, D.; Dai, Y.-C.; Yuan, W.-K. Characterization of surface oxygen complexes on carbon nanofibers by TPD, XPS and FT-IR. *Carbon* **2007**, *45* (4), 785–796.
- (34) Yamashita, T.; Hayes, P. Analysis of XPS spectra of Fe²⁺ and Fe³⁺ ions in oxide materials. *Appl. Surf. Sci.* **2008**, *254* (8), 2441–2449.
- (35) Grosvenor, A. P.; Kobe, B. A.; Biesinger, M. C.; McIntyre, N. S. Investigation of multiplet splitting of Fe 2p XPS spectra and bonding in iron compounds. *Surf. Interface Anal.* **2004**, *36* (12), 1564–1574.
- (36) Lazar, P.; Mach, R.; Otyepka, M. Spectroscopic Fingerprints of Graphitic, Pyrrolic, Pyridinic, and Chemisorbed Nitrogen in N-Doped Graphene. *J. Phys. Chem. C* **2019**, *123* (16), 10695–10702.
- (37) Nefedov, V. I.; Salyn, Y. V.; Leonhardt, G.; Scheibe, R. A comparison of different spectrometers and charge corrections used in X-ray photoelectron spectroscopy. *J. Electron Spectrosc. Relat. Phenom.* **1977**, *10* (2), 121–124.
- (38) Kim, K.; Adams, R. A.; Kim, P. J.; Arora, A.; Martinez, E.; Youngblood, J. P.; Pol, V. G. Li-ion storage in an amorphous, solid, spheroidal carbon anode produced by dry-autoclaving of coffee oil. *Carbon* **2018**, *133*, 62–68.
- (39) Maulana, A. Y.; Futalan, C. M.; Kim, J. MOF-derived FeF₂ nanoparticles@graphitic carbon undergoing in situ phase transformation to FeF₃ as a superior sodium-ion cathode material. *J. Alloys Compd.* **2020**, *840*, 155719.
- (40) Ma, D.-l.; Wang, H.-g.; Li, Y.; Xu, D.; Yuan, S.; Huang, X.-l.; Zhang, X.-b.; Zhang, Y. In situ generated FeF₃ in homogeneous iron matrix toward high-performance cathode material for sodium-ion batteries. *Nano Energy* **2014**, *10*, 295–304.
- (41) Li, L.; Meng, F.; Jin, S. High-Capacity Lithium-Ion Battery Conversion Cathodes Based on Iron Fluoride Nanowires and Insights into the Conversion Mechanism. *Nano Lett.* **2012**, *12* (11), 6030–6037.
- (42) Liu, P.; Vajo, J. J.; Wang, J. S.; Li, W.; Liu, J. Thermodynamics and Kinetics of the Li/FeF₃ Reaction by Electrochemical Analysis. *J. Phys. Chem. C* **2012**, *116* (10), 6467–6473.
- (43) Wang, F.; Kim, S.-W.; Seo, D.-H.; Kang, K.; Wang, L.; Su, D.; Vajo, J. J.; Wang, J.; Graetz, J. Ternary metal fluorides as high-energy cathodes with low cycling hysteresis. *Nat. Commun.* **2015**, *6* (1), 6668.
- (44) Huang, Q.; Pollard, T. P.; Ren, X.; Kim, D.; Magasinski, A.; Borodin, O.; Yushin, G. Fading Mechanisms and Voltage Hysteresis in FeF₂-NiF₂ Solid Solution Cathodes for Lithium and Lithium-Ion Batteries. *Small* **2019**, *15* (6), 1804670.
- (45) Lin, J.; Peng, H.; Kim, J. H.; Wygant, B. R.; Meyerson, M. L.; Rodriguez, R.; Liu, Y.; Kawashima, K.; Gu, D.; Peng, D. L.; Guo, H.; Heller, A.; Mullins, C. B. Lithium Fluoride Coated Silicon Nanocolumns as Anodes for Lithium Ion Batteries. *ACS Appl. Mater. Interfaces* **2020**, *12* (16), 18465–18472.
- (46) Zang, R.; Li, P.; Guo, X.; Man, Z.; Zhang, S.; Wang, C.; Wang, G. Yolk-shell N-doped carbon coated FeS₂ nanocages as a high-performance anode for sodium-ion batteries. *J. Mater. Chem. A* **2019**, *7* (23), 14051–14059.
- (47) Cosandey, F.; Al-Sharab, J. F.; Badway, F.; Amatucci, G. G.; Stadelmann, P. EELS Spectroscopy of Iron Fluorides and FeF_x/C Nanocomposite Electrodes Used in Li-Ion Batteries. *Microsc. Microanal.* **2007**, *13* (2), 87–95.
- (48) Wang, M.; Huai, L.; Hu, G.; Yang, S.; Ren, F.; Wang, S.; Zhang, Z.; Chen, Z.; Peng, Z.; Shen, C.; Wang, D. Effect of LiFSI Concentrations To Form Thickness- and Modulus-Controlled SEI Layers on Lithium Metal Anodes. *J. Phys. Chem. C* **2018**, *122* (18), 9825–9834.
- (49) Yao, K. P. C.; Kwabi, D. G.; Quinlan, R. A.; Mansour, A. N.; Grimaud, A.; Lee, Y.-L.; Lu, Y.-C.; Shao-Horn, Y. Thermal Stability of Li₂O₂ and Li₂O for Li-Air Batteries: In Situ XRD and XPS Studies. *J. Electrochem. Soc.* **2013**, *160* (6), A824–A831.
- (50) Chen, Y. C.; Ouyang, C. Y.; Song, L. J.; Sun, Z. L. Electrical and Lithium Ion Dynamics in Three Main Components of Solid Electrolyte Interphase from Density Functional Theory Study. *J. Phys. Chem. C* **2011**, *115* (14), 7044–7049.
- (51) Li, C.; Chen, K.; Zhou, X.; Maier, J. Electrochemically driven conversion reaction in fluoride electrodes for energy storage devices. *npj Comput. Mater.* **2018**, *4* (1), 22.

□ Recommended by ACS

Uniform Formation of a Characteristic Nanocomposite Structure of Biogenous Iron Oxide for High Rate Performance as the Anode of Lithium-Ion Batteries

Masakuni Takahashi, Jun Takada, et al.

JANUARY 24, 2023

THE JOURNAL OF PHYSICAL CHEMISTRY C

READ ▶

Phosphorus-Doped FeOF Nanoparticle-Based Cathodes for Lithium Storage

Hongyan Zhou, Youzhong Dong, et al.

SEPTEMBER 11, 2022

ACS APPLIED NANO MATERIALS

READ ▶

Fe³⁺-Derived Boosted Charge Transfer in an FeSi₂P₄ Anode for Ultradurable Li-Ion Batteries

Mahboobeh Nazarian-Samani, Kwang-Bum Kim, et al.

JULY 29, 2022

ACS NANO

READ ▶

Unveiling the Genesis and Effectiveness of Negative Fading in Nanostructured Iron Oxide Anode Materials for Lithium-Ion Batteries

Yun Seok Choi, Ji Man Kim, et al.

JANUARY 14, 2022

ACS NANO

READ ▶

Get More Suggestions >